



**HAL**  
open science

## **Multiaxial mechanical behavior of aramid fibers and identification of skin/core structure from single fiber transverse compression testing**

Judith Wollbrett-Blitz, Sébastien Joannès, Rémi Bruant, Christophe Le Clerc,  
Marc Romero de La Osa, Anthony R. Bunsell, Alba Marcellan

► **To cite this version:**

Judith Wollbrett-Blitz, Sébastien Joannès, Rémi Bruant, Christophe Le Clerc, Marc Romero de La Osa, et al.. Multiaxial mechanical behavior of aramid fibers and identification of skin/core structure from single fiber transverse compression testing. *Journal of Polymer Science Part B: Polymer Physics*, 2016, 54 (3), pp.374-384. 10.1002/polb.23763 . hal-01272319

**HAL Id: hal-01272319**

**<https://minesparis-psl.hal.science/hal-01272319>**

Submitted on 13 Feb 2023

**HAL** is a multi-disciplinary open access archive for the deposit and dissemination of scientific research documents, whether they are published or not. The documents may come from teaching and research institutions in France or abroad, or from public or private research centers.

L'archive ouverte pluridisciplinaire **HAL**, est destinée au dépôt et à la diffusion de documents scientifiques de niveau recherche, publiés ou non, émanant des établissements d'enseignement et de recherche français ou étrangers, des laboratoires publics ou privés.

# Multi-axial mechanical behavior of aramid fibers and identification of skin/core structure from single fiber transverse compression testing

JUDITH WOLLBRETT-BLITZ<sup>1,3,4</sup>, SÉBASTIEN JOANNÈS<sup>3</sup>, RÉMI BRUANT<sup>4</sup>, CHRISTOPHE LECLERC<sup>4</sup>, MARC ROMÉRO DE LA OSA<sup>4</sup>, ANTHONY BUNSELL<sup>3</sup>, ALBA MARCELLAN<sup>1,2</sup>

<sup>1</sup> ESPCI ParisTech, PSL - Research University, Laboratoire Sciences et Ingénierie de la Matière Molle, CNRS UMR CNRS 7615, 10 Rue Vauquelin, F-75231 Paris 5, France.

<sup>2</sup> Sorbonne Universités, UPMC Univ. Paris 06, UMR 7615, Laboratoire Sciences et Ingénierie de la Matière Molle, F-75005, Paris, France

<sup>3</sup> Mines ParisTech, PSL - Research University, Centre des Matériaux, CNRS UMR 7633, BP 87, 91003 Evry Cedex, France

<sup>4</sup> Manufacture Française des Pneumatiques Michelin, 23 Place des Carmes Déchaux, 63040 Clermont Ferrand Cedex 9, France

Correspondence to: A. Marcellan ([alba.marcellan@espci.fr](mailto:alba.marcellan@espci.fr))

## ABSTRACT

The transverse and longitudinal mechanical properties of aramid fibers like Kevlar 29 (K29) fibers are strongly linked to their highly oriented structure. Mechanical characterization at the single fiber scale is challenging especially when the diameter is as small as 15  $\mu\text{m}$ . Longitudinal tensile tests on single K29 fibers and Single Fiber Transverse Compression Test (SFTCT) have been developed. Our approach consists of coupling morphological observations and mechanical experiments with SFTCT analysis by comparing analytical solutions and finite element modeling. New insights on the analysis of the transverse direction response are highlighted. Systematic loading/unloading compression tests enable to experimentally determine a transverse elastic limit. Taking account of the strong anisotropy of the fiber, the transverse mechanical response sheds light on a skin/core architecture. More importantly, results suggest that the skin of the fiber, typically representing a shell of one micrometer in thickness, has a transverse apparent modulus of 0.2 GPa. That is around more than fifteen times lower than the transverse modulus of 3.0 GPa in the core. By comparison, the measured longitudinal modulus is about 84 GPa. The stress distribution in the fiber is explored and the critical areas for damage initiation are discussed.

**KEYWORDS:** Fiber, Aramid, Kevlar, Skin / Core structure, Single Fiber Transverse Compression Test

## INTRODUCTION

High performance para-aramid fibers, such as Kevlar® fibers, are designed for industrial challenges<sup>1-2</sup> that demand high strength and lightness such as is necessary for the low rolling resistance of tires, ballistic fabrics improvement or protection against cuts and abrasion. For these uses, Kevlar fibers are mainly exploited as threads, made of a bundle of twisted individual

fibers, or as woven in fabric which implies that the single fiber undergoes multi-axial mechanical loadings and complex contacts between fibers. In that context, understanding the mechanical responses at the single fiber scale in both longitudinal and transverse directions is crucial, and especially taking into account the property gradients between the extreme surface and the center of the fiber.

[Tapez ici]

However, few studies have dealt with the experimental mechanical analysis of the single fibers, particularly for low diameter fibers. Moreover, in contrast to the longitudinal properties, the transverse properties have received even much less attention.

The spinning process coupled with the intrinsic rigidity of the para-aramid monomer unit, leads to a highly oriented fibrillar structure resulting to a highly anisotropic mechanical behavior. Kevlar 29 is a relative low modulus aramid fiber compare to other grades as Kevlar 49 or Kevlar 149 grades. Hence, for the Kevlar 29, the longitudinal tensile modulus has been reported to be around 85 GPa<sup>1</sup> and the transverse modulus to be between 30<sup>3</sup> and 130<sup>4</sup> times lower. Such mismatch in the given values of the transverse properties arises from the experimental difficulty of accessing the fiber's transverse modulus. The experimental technique used in this study involves transverse compression of one single cylindrical fiber between two parallel flat platens and the measurement of the platen-relative displacement and the contact force on the fiber. This experiment is commonly called as "Brazilian" test or as Single Fiber Transverse Compression Test (SFTCT)<sup>5</sup>. Conducting such experiments on small diameter polymer fibers is challenging<sup>6</sup> because (1) their small diameter and low modulus make the test specimen very compliant per unit length, (2) tests require accurate alignment and measurement of platen displacement, especially taking account of displacement drifts during loading/unloading, (3) the experiment is sensitive to the geometry of the contact between fiber and platen<sup>4</sup> and consequently on variations in fiber diameter<sup>7</sup>. The SFTCT of Kevlar fibers has been investigated by several authors.<sup>3,4,6,8-11</sup> Phoenix and Skelton<sup>4</sup> pioneered this work with Kevlar 29 and 49, followed by Kawabata et al.<sup>3</sup> who studied transverse compression behavior of Kevlar 29, 49 and 149 fibers of diameters of around 12  $\mu\text{m}$ . Singletary et al.<sup>6,10</sup> investigated 1.5 and 6.0 denier Kevlar 29 fibers with diameters of 12  $\mu\text{m}$  and 24  $\mu\text{m}$  respectively. The experimental

[Tapez ici]

results reported there and more recently analyzed by Sockalingram et al.<sup>12</sup> using finite element (FE) models indicate that fibers exhibit nonlinear and inelastic response under large compression strains. To determine an estimate of the transverse elastic modulus, analytical linear elastic solutions have been proposed<sup>4,5,8,9</sup> and also modeled numerically considering an homogeneous material, a plane strain formulation and an elastic contact.<sup>6,10,12,13</sup> Experimental deviation from the elastic calculation has often been interpreted as a "pseudo-elastic stress limit". Thus, it has been defined numerically for a critical load,<sup>10,13</sup> corresponding to the compressive load per unit length normalized by the fiber diameter. Yet, yielding or transverse elastic limit could have been simply investigated experimentally by focusing on residual strain. As far as the authors know, it has never been done on Kelvar fibers.

Besides, numerous experimental studies<sup>1,14-17</sup> or recent works on molecular-level computations done by Grujicic et al.<sup>18-20</sup> have reported on the complexity of the hierarchical microstructure of the Kevlar fiber. The manufacturing process implies local gradient of shear rates and also complex kinetics of both cooling and solvent evaporation that modify the structure at the fiber diameter scale. The exact nature of the gradient of the microstructure within the fiber cross-section is still debated because clear evidence of microstructural changes with a such spatial resolution are extremely difficult to be obtained experimentally.<sup>14,21-27</sup> This gradient of fiber properties has often been schematized as a layered cylinder made of a "skin" and "core" structure.<sup>28</sup> The reported skin thickness varies with the experimental method used, but is of the order of 1  $\mu\text{m}$  for Kelvar 29, compared to a reported fiber diameter of 12  $\mu\text{m}$ . The microstructural descriptions of the Kevlar fiber converge on a transversally isotropic material at the center, and a more anisotropic structure at the surface.<sup>25</sup> The core is considered to be less oriented<sup>23</sup> with lower packing perfection<sup>15,25</sup> than the fiber surface because of a high concentration in chain ends.<sup>25</sup> The surface of

the fiber was considered as a 'barrier' to water sorption, implying lower diffusion coefficients in skin regions.<sup>29</sup> The skin is reported also to play a crucial role in slowing down any crack propagation process.<sup>26</sup> This skin/core effect is particularly strong for Kevlar 29 compared to other grades of Kevlar such Kevlar 49 or 129.<sup>30</sup> Singletary et al.<sup>10</sup> have discussed the potential of a SFTCT to probe the assumption of a skin/core effect at the fiber scale, but a skin/core structure was not included in their analysis of the test.

The main objective of this paper is to analyze the non-linear transverse compression response of a single para-aramid K29 fiber and to attempt to relate it to the fiber structure. To do so, the transverse mechanical response obtained experimentally by the Single Fiber Transverse Compression Test (SFTCT) will be analyzed in the light of numerical Finite Element Modeling (FEM) results and will reveal the skin/core structure so as to quantify the transverse mechanical properties. Despite a very complex hierarchical microstructure, as mentioned above, the present work will imply a continuum computational approach. Hence, apart from the presence of a skin/core structure, the modeled effective (i.e. homogeneous) material will not aim to feature microstructural elements.

The results and discussion are organized as follows: Firstly, the single fiber morphology will be described and the longitudinal behavior will be presented. Then, the experimental procedure of the developed SFTCT will be discussed and special attention will be paid to the definition of a transverse elastic domain by investigating experimentally the residual strain after crescent loadings. Existing analytical solutions and FEM results of transverse compression tests will be compared and will highlight the necessity to take into account the skin/core structure as to describe the non-linearity of the experimental load-displacement curves. Finally, the local stress field in the radial direction will be analyzed with respect to the observed damage mechanisms.

## EXPERIMENTAL

### Fibers and morphology characterization

The Kevlar fibers tested here were manufactured by DuPont and had a density of  $1440 \text{ kg.m}^{-3}$ . Fibers were extracted from a yarn of Kevlar 29 and are called K29 in this paper. Measurements of the diameter have been carried out by a Mitutoyo laser apparatus and a Scanning Electron Microscope (SEM) ZEISS DSM 982 GEMINI.

### Longitudinal Tensile Experiments

The dimensions of the fibers require special testing techniques to ensure the measurement in the appropriate range of stiffness. Single fiber tensile tests were performed on the universal fiber tester.<sup>31</sup> This device has been extensively used to study a wide range of textile and technical fibers<sup>32,33</sup> but also for natural organic fibers such as silk.<sup>34</sup>

The fiber was held horizontally between two clamps, one was fixed and the other was connected to a movable cross-head supplied with a load cell. To avoid slippage of the fiber inside the jaws, the fiber was tied by clove hitches and the gauge length was fixed at 30 mm. The displacement of the cross-head was controlled by a LVDT transducer. The resolution of the load and the displacement were respectively 0.1 g (Sensotec load cell of 2.5 N) and 0.01% (LVDT sensor from Sensotec). A constant strain rate was imposed at  $0.0043 \text{ s}^{-1}$ . The tests were conducted at  $21^\circ\text{C}$  and 50% relative humidity. Such a tensile test required testing at least 30 fibers to ensure statistical reproducibility.

### Single Fiber Transverse Compression Test (SFTCT)

The transverse compression test consisted of compressing diametrically a circular disk<sup>35</sup> or right-circular cylinder of material between two parallel and rigid plates. Applied to fibers, this experiment is also known as the Single Fiber Transverse Compression Test (SFTCT).<sup>5,36</sup>

Here, transverse mechanical properties have been characterized using an apparatus that was

[Tapez ici]

initially designed by Creton et al.<sup>37</sup> to quantify adhesion of pressure sensitive adhesives. Developments on the initial setup were carried out so as to decrease the overall compliance of the apparatus and to enhance its sensitivity so as to perform transverse compression test on single fibers.

As shown in figure 1, the K29 fiber was compressed between a glass probe (1) and a sapphire plate (2). The upper plate was made of sapphire, chosen for its high modulus and its transparency, so the test could still be followed using the camera located on the upper side (objective Zeiss x20, 100 frames/s). The sapphire plane plate 14 mm diameter, 3 mm thick obtained from UQG Optics® was mechanically fixed in a metallic holder. The glass probes were bought from Hellma-Optik® (1 mm diameter, 1.5 mm thickness) and glued by cyanoacrylate glue (Sader). It is appropriate to assume that the plates were rigid relative to the polymer fiber, leading to a contact problem in the analysis of the plane strain compression of a cylinder between rigid and parallel plates. The design of the device was conceived so as to ensure a compression cycle (loading/unloading) avoiding any drift in displacement during the experimental procedure. For that purpose the displacements of the two plates were controlled by independent motors.

As described in figure 1, the displacement of the lower glass probe was monitored by the central stepping motor at a constant velocity of  $1 \mu\text{m}\cdot\text{s}^{-1}$  until a defined maximum load  $F_{max}$ . The three external stepping motors controlled the movement of the upper plate (at  $1 \mu\text{m}\cdot\text{s}^{-1}$ ), so as to control the unloading, and to ensure a perfect parallelism of the two probe surfaces. Thus, the alignment was adjusted by the three lateral motors using the optical fringes observed by the microscope. The motors were bought from Physik Instrumente and are linked to a load cell (Measurement Specialties) with a precision of 5 mN, the optical fiber was bought from Philtec (D63-LPT) and insure a precision of 60 nm.

A systematic estimation of the compliance of the device (compression test without fiber) was

[Tapez ici]

carried out before and after each fiber test that enabled the correction of the raw displacement measurements and to estimate the displacement undergone by the fiber. Moreover, if the measured compliances before and after fiber testing were not perfectly superimposed, the test was not considered valid. Indeed, such a discrepancy could indicate artifacts such as slippage or misalignment of the probes during the test.

SFTCT were conducted at room temperature without humidity control. For each condition, a minimum of 30 tests were performed.

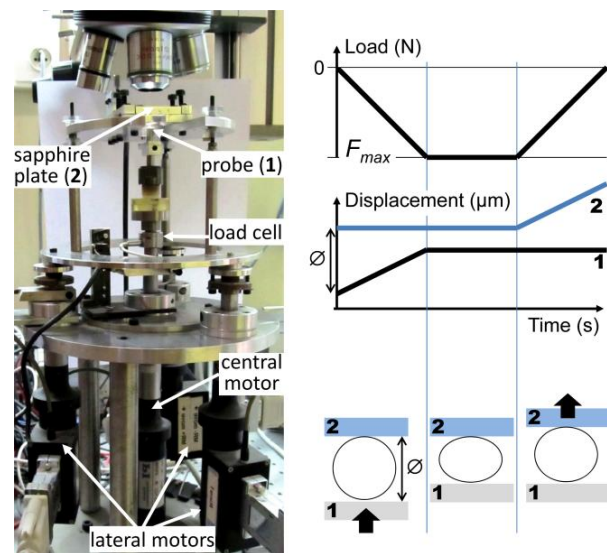


FIGURE 1 Schematic steps of a transverse compression test using the experimental apparatus. Displacement of probe (1) was monitored to a maximum load,  $F_{max}$ , here -1 N, then a delay of less than 1 sec was applied before moving probe (2).

### Numerical experiment of the Single Fiber Transverse Compression Test

Numerical analysis allowed accessing material parameters that are not easily accessible by the Force – Displacement signal from a mechanical test on a complex geometry. A Finite Element Model (FEM) of the transverse compression test is, in some ways, a virtual test, that makes the stress state in the cross-section accessible throughout the compressive loading. By fitting the experimental load curves, FEM enabled to

virtually visualize the stress fields, but also to go a step further and to assess the material properties in terms of effective transverse modulus and behavior.

The finite element solver used in this study is called ZeBuLoN<sup>®</sup> and is a package included in the Zset<sup>®</sup> suite computing solution (<http://zset-software.com/>).

The digital fiber was drawn with the experimentally obtained radius and the skin/core organization incorporated into the geometry. Modeling the SFTCT was a plane strain problem since the contact length was about 1 mm, seventy times greater than the diameter.

Moreover, given the geometrical, physical and mechanical symmetries, only a quarter of the fiber needed to be modeled. A contact was defined between the plate and the surface of the fiber. The contribution of friction due to the tangential slippage at the interface was estimated numerically and shown to be negligible. The same conclusion arises from the work of Sockalingram et al.<sup>12</sup> who reported that the difference in the maximum true compressive stress (at a nominal strain of 40% - AN) with and without friction was less than 3%. Thus, the fiber/probe contact was reduced to a normal contact.

A vertical displacement was imposed on the plate and the resulting force from the compression of the fiber digitally evaluated. The fiber section was meshed by linear quadrangles in order to make the calculation of nodal reactions of the contact zone possible.

To reproduce the experimental test, the upper plate was considered to be sapphire, assumed to be purely elastic and isotropic with an elastic Young's modulus  $E = 345$  GPa and a Poisson ratio  $\nu = 0.25$ . It was verified that the replacement of sapphire with glass ( $E = 70$  GPa,  $\nu = 0.2$ ) has no influence on the numerical results. Sapphire and glass may both be considered as infinitely rigid compared to the transverse behavior of the K29 fiber. The K29 behavior was initially considered to be transversely isotropic and linearly elastic in both skin and core regions.

## RESULTS AND DISCUSSION

### Single fiber morphology

Geometry and surface state of the fiber are crucial for the analysis of the transverse mechanical properties. A morphological study was carried out first, focusing on cross-section of an embedded bundle of fibers. Fiber cross-section analysis (SEM images) confirmed the cross-section circularity of the fibers and statistical analysis, over more than 300 measures, revealed a mean fiber diameter of  $14.5 \mu\text{m}$  comprised between  $14.3 \mu\text{m}$  and  $14.7 \mu\text{m}$  at a 95% confidence level. A similar average diameter was obtained with the laser scan micrometer but the confidence interval was a little wider since the standard deviation was around  $0.3 \mu\text{m}$  for more than 100 values. SEM observations of the fiber surface similarly confirmed the right-circular cylindrical shape. As shown in figure 2a, the K29 surface appeared relatively smooth. The diameter was measured from the fiber's edges along the same fiber. The fiber diameter dispersion was about the same order of magnitude as the inter-fiber dispersion, typically of  $\pm 0.1 \mu\text{m}$  at a 68% confidence for a length scale of 30 mm and over 100 measurements. This corresponds to 1.4% of the diameter. Such dispersion is relatively low compared to other polymer fibers.<sup>38</sup> For shorter length scales, typically around 1 mm, the fiber diameter could be considered as constant.

As shown in figure 2a, the K29 surface appeared with a few scattered defects with typical size of  $\sim 0.1 \mu\text{m}$  that were associated with extrinsic material due to environmental dust contamination.

A second population of defects that possibly could result from handling was observed, as in figure 2b, implying  $\sim 1 \mu\text{m}$  length-scale delamination. The revealed fibrillated structure seemed to proceed by the peeling or delamination of the first micrometer of the fiber surface and revealed an apparent core/shell structure. This type of defect was observed several times but less frequently than

[Tapez ici]

the first type. Typically around 10% of the observed fibers exhibited such feature with a delaminated length of 200  $\mu\text{m}$  and a periodicity of 10 mm. The Figure 2c revealed also the highly oriented microstructure along the fiber axis. Bundles of fibrils were clearly observed with thickness of  $\sim 50\text{--}100\text{ nm}$  as observed by AFM<sup>27</sup>. Note that this characteristic length scale

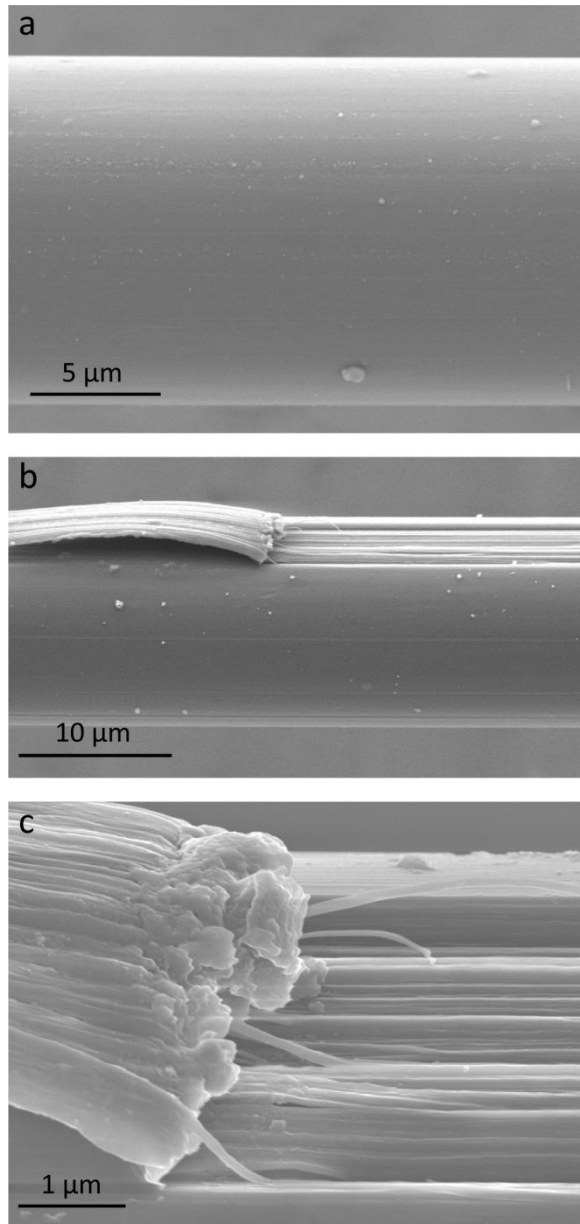


FIGURE 2 SEM images of the as-received K29 fiber surface (a) and a representing the peeling or delamination of fiber skin (b). Enlargement of

[Tapez ici]

image (b) is given in (c). The skin width is estimated to be of 1  $\mu\text{m}$ -thick.

is more than two orders of magnitudes lower than the fiber diameter scale and accounts for the modeling approach of two homogenized phases that will be detailed in a next section. The thickness of the 'skin' has been estimated from the observations as being approximately 1  $\mu\text{m}$  which is in agreement with the skin thicknesses that have been reported elsewhere.<sup>14,15</sup>

### Longitudinal Experiments results

Longitudinal behavior was determined by monotonic tensile tests (30 tests per conditions). The typical stress strain curve is represented in the figure 3. Results gave a longitudinal Young modulus  $E = 84 \pm 4\text{ GPa}$ , a failure strain  $\epsilon_R = 4.0 \pm 0.6\%$  and a failure stress  $\sigma_R = 3.3 \pm 0.2\text{ GPa}$ . The tangent modulus was seen to increase by 15% with applied strain from 84 GPa to 95 GPa, revealing a progressive alignment of macromolecules.

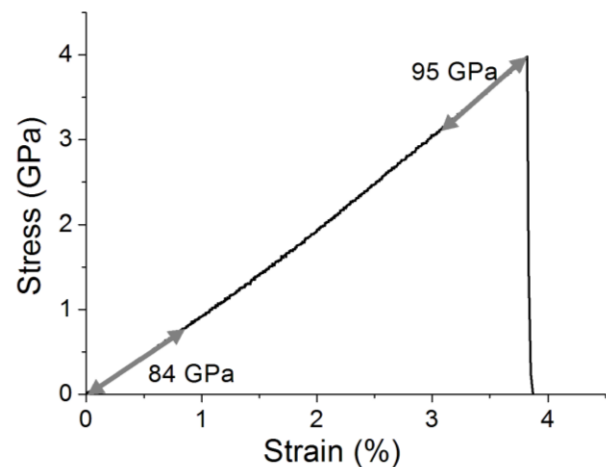


FIGURE 3 Median profile of a tensile curve, longitudinal tensile test, K29.

### Transversal behavior: Force-displacement response of SFTCT

The compliance  $C$ , of the developed SFTCT equipment was measured (without fiber) with a

good reproducibility as  $0.37 \pm 0.02 \mu\text{m}\cdot\text{N}^{-1}$ . Load-displacement curves of two compliances C1 and C2, corresponding respectively to the compliance of the device before and after fiber test are plotted in the figure 4. The transverse compression (and unloading) of the K29 fiber exhibited the expected dissipative behavior that has been often reported in the literature. From this testing procedure, raw displacement was systematically corrected by the compliance of the device. The initial diameter of the fiber could be measured with a very good accuracy as the difference in raw displacement between the compliance and the fiber signal, as shown in figure 4. As a control experiment, the fiber diameters were first estimated by the SFTCT equipment and then were measured by SEM observations. Values were in perfect agreement, strengthening the assumption of robustness of the experimental procedure. Note that for such a fine initial diameter, the contact width was too small to be analyzed quantitatively by optical microscopy.

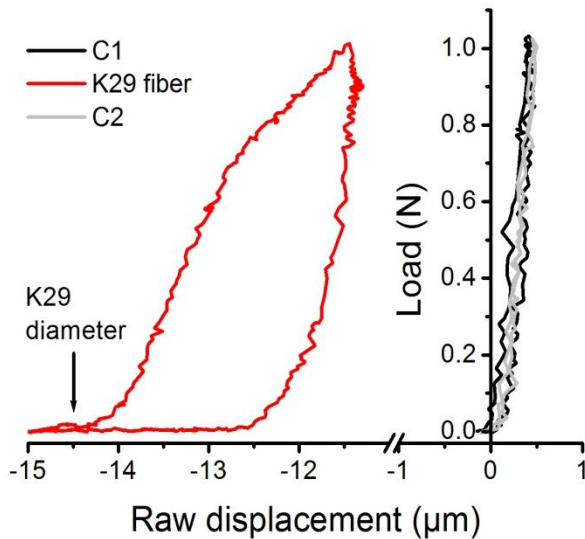


FIGURE 4 Experimental protocol for transverse compression test: the steps were successively device compliance C1, single K29 fiber and then device compliance C2.

So as to examine the reversibility of the deformation mechanisms, the fiber was submitted to loading/unloading compression experiments. Experimental curves of the SFTCT

are presented in figure 5. From a phenomenological point of view, the non-linearity of the Force–displacement signal revealed the complex stress state and contact between the cylindrical fiber and the two parallel probe surfaces, as shown in figure 6.

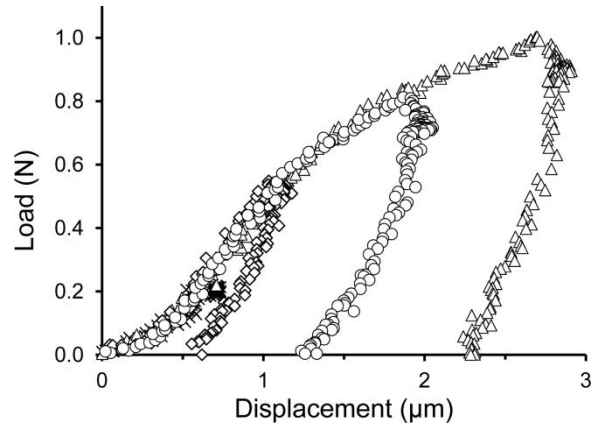


FIGURE 5 First transverse loading/unloading cycles for different maximum loads.

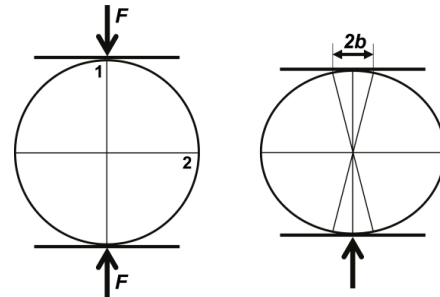


FIGURE 6 Schematic views of the geometry with  $b$  defined as the contact half-width and  $F$  the applied load normalized by the compressed length. 1 and 2 directions are defined in the scheme.

### Transverse elastic limit

Whereas other studies have defined the transverse elastic limit by the onset of deviation from Hertzian contact models<sup>10</sup>, here residual displacement after unloading was considered as an experimental criterion of yielding. The residual strain, expressed as the residual displacement normalized by the fiber diameter, has been plotted as a function of the maximal applied load in figure 7. For each condition,

[Tapez ici]

experiments were repeated 20 times, eliminating tests for which C1 and C2 compliances were not perfectly superimposed. The elastic limit was estimated to be around  $0.25 \pm 0.05 \text{ N.mm}^{-1}$ . Below this value, the loading/unloading SFTCT presented no residual displacement and a very weak hysteresis, strengthening the assumptions of a frictionless contact condition and of a rather homogenous stress concentration along the 1 mm contact. Interestingly, the corresponding yielding strain at  $0.25 \text{ N.mm}^{-1}$  is around  $6 \pm 1\%$  which seemed to be in line with what has been reported elsewhere for K29 fibers.<sup>3,10</sup>

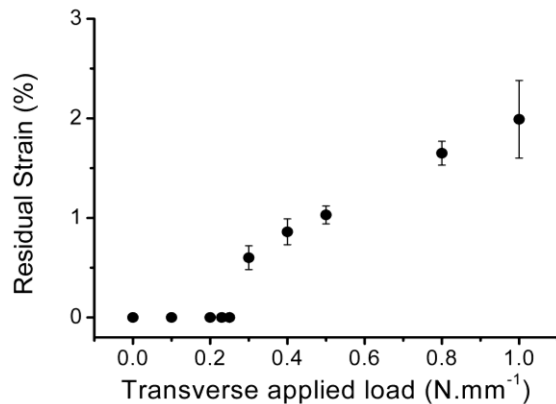


FIGURE 7 Transverse residual strains after a transverse compression test at different maximum distributed loads (20 tests per conditions – errors bars correspond to standard deviation). Residual strain was estimated by normalizing the residual displacement by the initial diameter of the fiber.

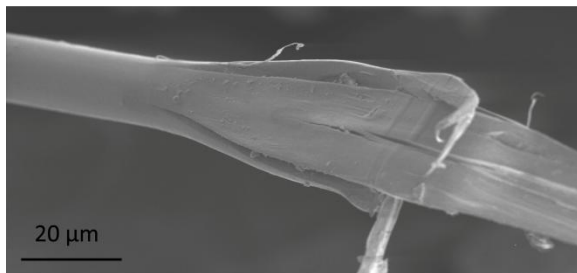


FIGURE 8 SEM observation of a fractured surface. The fiber tested was submitted to a SFTCT above the determined elastic limit at  $1 \text{ N.mm}^{-1}$  and then fractured in tension. Fracture systematically occurred in the compressed region, see flattened shape of the

[Tapez ici]

fiber. Note that fracture proceeded by two planes, perpendicularly and parallel to the platen.

No evidence of permanent deformation was observed by SEM within the defined transverse elastic regime. In contrast, above  $0.25 \text{ N.mm}^{-1}$ , fibers exhibited a flattened shape as shown in figure 8.

### Analytical solution of transverse compression tests and comparison with FEM simulation

The non-linearity response of a transverse compression test has been highlighted for aramid fibers<sup>3,4,6,10,13</sup> and different analytical expressions have been developed to estimate the transverse modulus.<sup>4,8,9,39</sup> The general approach consisted of using the load-displacement measurements in conjunction with the small strain analytical solution based on the Hertzian contact models between parallel plates.<sup>5,39</sup> The problem is considered to be purely elastic and meets the assumptions of plane strain. Hertz's resolution has been extended by Mc Ewen<sup>39</sup> to account for the effect of tangential friction. Simultaneously, Timoshenko and Goodier<sup>40</sup> derived the stress solution for a whole cylinder under compression with concentrated loads. By combining these two approaches and neglecting friction in the contact zone of SFTCT problems, Phoenix and Skelton<sup>2</sup> followed by Abdul Jawad et al.<sup>8</sup> provided in the 1970s very similar expressions of the relative displacement of the probes as a function of the applied load and the transversely isotropic properties of the fibers. Singletary et al.<sup>10</sup> reported that those two models predict identical stress distributions which is perfectly justified when the width of the contact zone is considered very small compared to the radius of the fiber and the longitudinal young modulus is very high compared to the radial modulus. In that case, the two models are reduced to a single simplified expression. Table 1 reports those three analytical models that have been proposed and used for SFTCT in the literature.

Abdul Jawad et al.<sup>8</sup> considered a concentrated load on one side and a distributed load on the other, whilst Phoenix et al.<sup>4</sup> considered a distributed load on a generator for the two planes, respectively given in (1) and (2). They both used the stress superposition procedure which is justified for a contact of semi-infinite elastic solids, i.e. when the contact width,  $2b$  is small compared with the cylinder radius, see figure 6. Expression (3) from Singletary et al.<sup>10</sup> is the simplified expression, which in the context of aramid fibers, gives the same results as expressions (1) or (2). Relations (1), (2) and (3) thus provides the transverse displacement  $U_1$  ( $\mu\text{m}$ ) as a function of the applied load normalized by the compressed length  $F$  ( $\text{N}\cdot\text{mm}^{-1}$ ) and depends on the radius  $R$  ( $\mu\text{m}$ ), half-width of the contact  $b$  ( $\mu\text{m}$ ), the transverse modulus  $E_1$  (MPa), longitudinal modulus  $E_3$  (MPa) and the Poisson's ratios  $\nu_{12}$  and  $\nu_{13}$ .

The compliance matrix for a general elastic behavior considering orthotropy, is given by (4):

$$(4) \quad \begin{pmatrix} S_{11} & S_{12} & S_{13} & S_{14} & S_{15} & S_{16} \\ S_{21} & S_{22} & S_{23} & S_{24} & S_{25} & S_{26} \\ S_{31} & S_{32} & S_{33} & S_{34} & S_{35} & S_{36} \\ S_{41} & S_{42} & S_{43} & S_{44} & S_{45} & S_{46} \\ S_{51} & S_{52} & S_{53} & S_{54} & S_{55} & S_{56} \\ S_{61} & S_{62} & S_{63} & S_{64} & S_{65} & S_{66} \end{pmatrix} = \begin{pmatrix} 1/E_1 & -\nu_{12}/E_1 & -\nu_{13}/E_1 & 0 & 0 & 0 \\ -\nu_{12}/E_1 & 1/E_2 & -\nu_{23}/E_2 & 0 & 0 & 0 \\ -\nu_{13}/E_1 & -\nu_{23}/E_2 & 1/E_3 & 0 & 0 & 0 \\ 0 & 0 & 0 & 1/G_{23} & 0 & 0 \\ 0 & 0 & 0 & 0 & 1/G_{13} & 0 \\ 0 & 0 & 0 & 0 & 0 & 1/G_{12} \end{pmatrix}$$

with direction 3 corresponding to the fiber axis.

Note that assuming transverse isotropy gives:

$$E_1=E_2, \nu_{13}=\nu_{23}=\nu_{31} \cdot E_1/E_3, G_{13}=G_{23} \text{ and}$$

$$G_{12}=E_1/2(1+\nu_{12}).$$

Hadley et al.<sup>5</sup> derived an expression for  $b$ , the contact half-width, schematized in figure 6, considering a change in curvature of the geometry from  $1/r$  to zero at the contact zone. This expression written for a transversely isotropic elastic material being compressed between two infinitely rigid plates is in agreement with the result of Hertz. The square of the contact half-width is a linear function of the force per unit length given by<sup>5</sup>:

$$b^2 = \frac{4FR}{\pi} (S_{11} - S_{13}^2/S_{33}) \quad (5)$$

Using these different expressions, several values of the K29 transverse modulus were

reported from 0.77 GPa<sup>4</sup> by Phoenix and Skelton, around 2.50 GPa<sup>10,11</sup> for Singletary et al. and up to 2.59 GPa<sup>3</sup> for Kawabata.

Using coefficients given by Table 2, the analytical solutions were compared in the elastic domain, i.e. up to 0.25 N.mm<sup>-1</sup>, to the FE simulation response. For homogeneous transversely isotropic material and with a small strain formulation, the FE modeling was perfectly superimposed to the analytical results. At 0.25 N.mm<sup>-1</sup> the difference between a small strain and a finite strain formulation for the computed displacement is less than 0.02  $\mu\text{m}$  which can be considered negligible.

TABLE 1 Analytical models for the single fiber transverse compression test, assuming transverse isotropy.

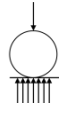
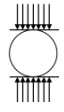
$U_1 = -\frac{4F}{\pi} \left( (S_{11} - S_{13}^2/S_{33}) (\text{arcsinh}(R/b) + 0.69) \right) + \frac{2F}{\pi} (S_{11} + S_{12} - 2S_{13}^2/S_{33}) - \frac{4F}{\pi} \left( (S_{12} - S_{13}^2/S_{33}) (R/b) \left( \sqrt{1 + (R/b)^2} - R/b \right) \right)$ <p>from Abdul Jawad et al.<sup>8</sup></p>	(1)	
$U_1 = -\frac{4F}{\pi} \left( (S_{11} - S_{13}^2/S_{33}) (\text{arcsinh}(2R/b)) \right) + \frac{2F}{\pi} (S_{11} + S_{12} - 2S_{13}^2/S_{33}) - \frac{4F}{\pi} \left( (S_{12} - S_{13}^2/S_{33}) (2R/b) \left( \sqrt{1 + (2R/b)^2} - 2R/b \right) \right)$ <p>from Phoenix et al.<sup>4</sup></p>	(2)	
$U_1 = -\frac{4F}{\pi} S_{11} \left( 0.19 + \text{arcsinh} \sqrt{\frac{\pi R}{4FS_{11}}} \right)$ <p>From Singletary et al.<sup>10</sup></p>	(3)	

TABLE 2 Elastic parameters used for FEM and local parameter sensitivity on  $U_1$  estimated at a distributed load of 0.25 N.mm<sup>-1</sup>.

Parameters		$\Delta U_1$ ( $\mu\text{m}$ )	Relative sensitivity
$E_3$	84 GPa (measured)	0.0003	0.3%
$R$	7.25 $\mu\text{m}$ (measured)	0.0150	20.5%
$E_1=E_2$	optimized	0.0573	78.4%
$\nu_{31}$	0.6 from refs. 6,13	0.0006	0.7%
$\nu_{12}$	0.2 from refs. 13, 41	$\leq 10^{-6}$	0.02%

[Tapez ici]

$G_{13} = G_{23}$  1.8 GPa from refs. 42,43 - -

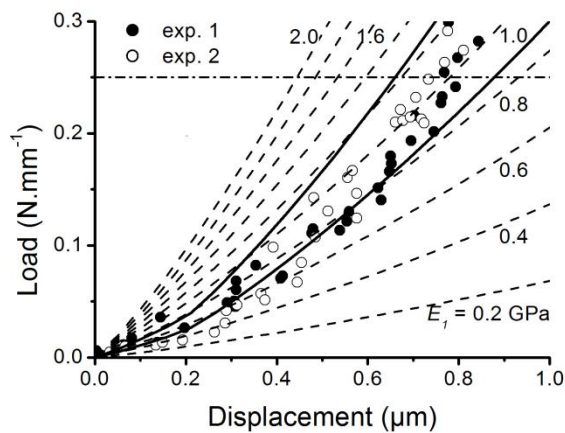


FIGURE 9 Calculated loads from analytical models (dashed lines) using eq. 1-3 are compared to 2 experimental results (dots). Using elastic parameters given in Table 2, transverse modulus,  $E_1$  was varied from 0.2 to 2 GPa by 0.2 GPa increments. Note that FEM assuming a homogeneous material and a small strain formulation gave rise to a perfect superposition for such range of investigated moduli. Solid lines refer for calculation accounting a fiber with an average diameter of 14.5  $\mu\text{m}$  but varying from 14.4 to 14.6  $\mu\text{m}$  on the 1 mm length of the test, using  $E_1$  of 1.0 and 1.5 GPa, respectively. Experimental transverse elastic limit of 0.25  $\text{N}\cdot\text{mm}^{-1}$  was given as a guideline.

The assumption of transverse isotropic elasticity for the FE calculation requires five independent elastic parameters and an accurate estimate of the initial radius of the fiber. Indeed, as shown in table 2, parameter sensitivity was estimated numerically by considering a 10% deviation of each parameter and calculating its impact on the displacement ( $\Delta U_1$ ) for a given  $F$ , here 0.25  $\text{N}\cdot\text{mm}^{-1}$ . For this local sensitivity analysis,  $E_1$  has been arbitrarily fixed at 1.0 GPa. As expected, only  $E_1$  and  $R$  have a significant impact on the calculation.

The analytical models and FE calculations were conducted by fixing parameters that can be

obtained from our experiments with  $E_3=84$  GPa (from longitudinal tensile tests),  $2R=14.5$   $\mu\text{m}$  (from the initial distance between the 2 probes) and other parameters were obtained from literature:  $\nu_{31}=0.6$ <sup>13,6</sup>,  $\nu_{12}=0.25$ <sup>13,41</sup> and  $G_{13}=1.8$  GPa.<sup>42-43</sup> A series of transverse moduli comprised between 0.2 and 2 GPa was tested in order to fit the experiment. Estimation of the transverse modulus from these curves appeared difficult and highlighted the discrepancies that have already been reported in literature. Part of the explanation might come from the uncertainty of the displacement range that has to be considered.

Note that calculations were carried out for a wide range of transverse moduli but none of these calculations were capable of fully satisfying the experimental response as the general shape of the Force-displacement is not well described. It appeared that several values may be valid depending on the region of the curve considered. As discussed previously, the first stages of the fiber compression are extremely difficult to control because of the high experimental sensitivity as the fiber diameter, the platen alignment or the presence of surface asperities could induce contact heterogeneities along the fiber length.

From our SEM characterization of the fiber, diameter dispersion was estimated at  $\pm 0.1$   $\mu\text{m}$ . Thus, in the most unfavorable case, it can be assumed that the full contact of the fiber length was obtained for a maximum of 0.2  $\mu\text{m}$ -displacement. By reverse engineering, keeping the assumptions of a homogeneous transversely isotropic material, calculations were carried out to estimate the impact of a defect of a  $\pm 0.1$   $\mu\text{m}$ -length scale. In figure 9, we considered a fiber having an average diameter of 14.5  $\mu\text{m}$  but varying from 14.4 to 14.6  $\mu\text{m}$  on the 1 mm length of the test. Solid lines surrounded experimental values by using transverse moduli of 1.0 and 1.5 GPa, respectively. As shown in figure 9, this hypothesis improved the curvature of the calculation but did not account for the experimental Force-displacement response after 0.2  $\mu\text{m}$ . Thereby, it seemed unrealistic

[Tapez ici]

that the curvature of the SFTCT came only from the establishment of contact.

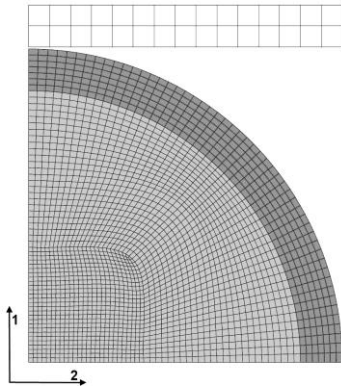


FIGURE 10 Mesh used for the Finite Element simulation accounting for a sharp arbitrary skin/core interface. White: Half of the upper platen, dark grey: Skin of the fiber, light grey: Core of the fiber.

#### FEM of skin/core structure and stress field

The accuracy of the numerical response has been significantly improved and adequately described using a skin/core structure, both considered as transversely isotropic. Our approach consisted of fixing a mesh structure that has been refined by adding a skin/core architecture, as pictured in figure 10. Hence, as shown by SEM, a  $1\ \mu\text{m}$ -skin was clearly identified, see figure 2. Such a size appeared relevant for K29.<sup>14,44,45</sup>

The results of the FE modeling are given in figure 11. The non-linearity experimentally observed is better adjusted with a layered material. The transverse skin and core moduli were optimized to obtain the best agreement with the experimental data. Effective values were established at 0.2 GPa and 3.0 GPa, respectively for the skin and the core. Note that due to the small value of the skin transverse modulus compared to those of the core and the upper plate, a finite strain formulation has been used. The effective values indirectly integrate the skin/core transition zone. Interestingly, the

3.0 GPa obtained for the transverse modulus in the core is very close to the value reported by Grujicic et al.<sup>20</sup> using a molecular-level approach. Furthermore, it is worthwhile to comment on the robustness of the obtained solutions. In fact, by varying the skin and core moduli from the optimized values, respectively 0.2 GPa and 3.0 GPa, it is very difficult to keep a good force-displacement agreement. Also by slightly varying the skin thickness, the 3.0 GPa value is found to be rather insensitive as a variation of 10% of the skin thickness induces only 5% variation on the displacement prediction (at  $0.25\ \text{N}\cdot\text{mm}^{-1}$ ) and this is typically of the order of the experimental scatter.

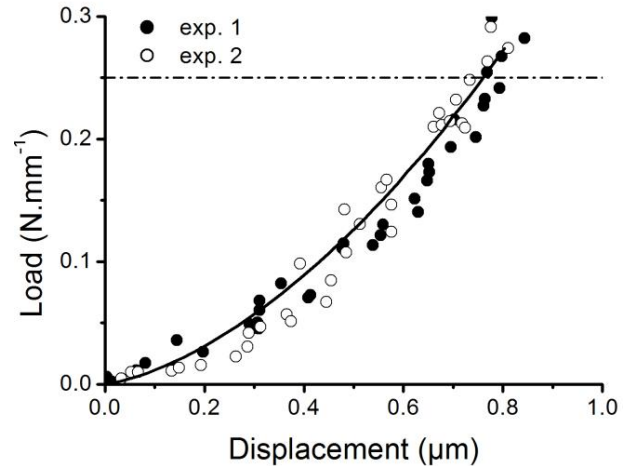


FIGURE 11 Force-displacement curves of the experimental transverse compression in the elastic domain (dots), of the FE simulation with a skin/core structure  $E_{1,core}=3.0\ \text{GPa}$ ,  $E_{1,skin}=0.2\ \text{GPa}$  (solid line). Experimental transverse elastic limit of  $0.25\ \text{N}\cdot\text{mm}^{-1}$  was given as a guideline.

The cross-sectional stress field, in a radial coordinates, at a distributed load of  $0.25\ \text{N}\cdot\text{mm}^{-1}$ , is shown in figure 12. The contour map information is completed by isolines in order to better reflect the multi-axiality of the stress field. In the first quadrant (top right), the hoop stress  $\sigma_{\theta\theta}$  is plotted and the range lies between -51 to 11 MPa. As expected, the tensile stress is confined in a small area along the vertical

[Tapez ici]

direction and near the center of the cross-section which is also the highest loaded place for the core. Larger values, induced by the compressive load, can be seen along the horizontal axis. In addition, a highly compressed area also appears near the loading boundary. The presence of skin is clearly visible since a strong stress gradient of the hoop stress appears at the upper interface with the core. As will be mentioned later, this stress discontinuity at the skin/core interface cannot be observed either for the radial stress or for the shear stress. This reflects a parallel or series combination of the skin and the core. This strong stress gradient between the skin and the core is amplified by the hypothesis of two homogeneous phases perfectly bonded.

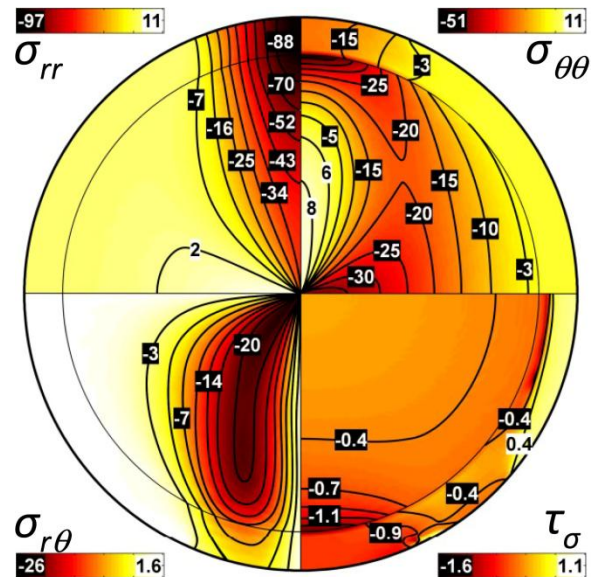


FIGURE 12 Stress Fields in the different directions. Up left:  $\sigma_{rr}$ , up right:  $\sigma_{\theta\theta}$ , down left:  $\sigma_{r\theta}$  and down right:  $\tau_{\sigma} = \frac{Tr(\underline{\underline{\sigma}})/3}{\sigma_{eq}}$ , with  $\sigma_{eq}$ , the von Mises equivalent stress and the  $Tr(\underline{\underline{\sigma}})/3$  term being the hydrostatic pressure or the equi-triaxial stress.

The second quadrant (top left) shows the special distribution of the radial stress state  $\sigma_{rr}$ . As for the hoop stress, a value of 11 MPa was found at the center of the cross-section. The compressive stress of 97 MPa was confined to

[Tapez ici]

the region between the contact area and the center without any discontinuity at the skin/core interface. In absolute values the compressive stresses were far higher than the longitudinal tensile strength of the fiber. As shown in figure 8 for a significant compressive load, fracture occurred systematically in the 1 mm compressed length. This particular fracture morphology seemed to reveal a high sensitivity to the opening principal stress. Thus, one fracture plane was observed to proceed perpendicular to the platens.

The shear stress  $\sigma_{r\theta}$  is shown in the third quadrant (bottom left). The stress range goes from -26 to 1.6 MPa and is almost negative; a negative shear would cause a counter-clockwise rotation of the infinitesimal element about the element center. The shear stress is minimal (maximum absolute value) in the core of the fiber and a shear stress continuity is observed at the interface with the skin.

The fourth quadrant is very instructive since it presents the stress triaxiality distribution over the fiber cross-section. The local triaxiality ratio  $\tau_{\sigma}$  is defined as:

$$\tau_{\sigma} = \frac{Tr(\underline{\underline{\sigma}})/3}{\sigma_{eq}} \quad (6)$$

with the  $Tr(\underline{\underline{\sigma}})/3$  term being the hydrostatic pressure or the equi-triaxial stress and  $\sigma_{eq}$ , the von Mises equivalent stress.

This load independent indicator is known to greatly influence the amount of plastic strain which a material may undergo before ductile failure occurs.<sup>46</sup> Pure shear would induce a zero triaxiality whereas for an uniaxial tension  $\tau_{\sigma} = 0.33$ , for a transverse plane strain load  $\tau_{\sigma} = 0.58$  and  $\tau_{\sigma} = 0.67$  for an equibiaxial tension state of stress. From figure 12, the triaxiality ratio ranges between -1.6 and 1.1. The positive stress triaxiality is associated with a volume change and is often used as an indicator for the modeling of void growth in ductile solids. Apart from the contact zone which is a disturbed area, the stress triaxiality is relatively low; the higher absolute value is visible at the interface between the core and the skin. Note that as observed in figure 8, this region corresponds to

a crack plane. Another stressed region appears quite close to the interface area inside the skin. This sharp gradient could be the cause of a number of damage mechanisms. It is interesting to note that a probable mesophase region between the skin and the core may also be the more affected area. The fiber structure is, according to some authors, defined as a triphasic structure, a crystalline core, an amorphous skin and a mesophase representing from 20%<sup>47,48</sup> to 40%<sup>44</sup> of the whole volume. By its constitution and the complex multi-axial stress field, the mesophase area could be a preferential location for damage initiation.

## CONCLUSION

The combination of morphological observations and single fiber transverse compression experiments coupled with the use of the FE simulation appeared as a promising approach for the study of the single fiber structure. By coupling mechanical and numerical studies, the heterogeneous structure of the fiber has been revealed in this work and a skin/core architecture shown to be required to reproduce the experimental elastic response. Assuming a skin of 1  $\mu\text{m}$  thickness, the transverse elastic effective moduli of the core and skin were defined to be 3.0 GPa and 0.2 GPa respectively. A transverse elastic limit was established experimentally by probing systematically the residual strain after loading/unloading cycles. Typically above  $0.25 \pm 0.05 \text{ N}\cdot\text{mm}^{-1}$ , yielding processes operate, leading to a strong strain energy dissipation and an irreversible flattening of the fiber. At the elastic limit, the stress fields were analyzed and revealed a stress concentration all along the compression axis and mostly at the skin/core interface because of the skin/core mismatch of transverse moduli. The adopted approach opens interesting perspectives. Above the elastic limit a detailed description in comprehension of the single fiber mechanical response should be further studied.

## ACKNOWLEDGEMENTS

The authors like to specifically thank Michelin for the financial support. The authors thank Yves Favry and Maria Betbeder (Mines ParisTech) and Dr. D. Martina (ESPCI ParisTech) for their technical support. They also thank J.-L. Halary (ESPCI ParisTech) for numerous helpful discussions and advices on microstructure and deformation mechanisms.

## REFERENCES AND NOTES

1. H. Yang, Kevlar aramid fibre; Wiley: New York, **1993**.
2. J. Kim, W.G. McDonough, W. Blair, G.A. Holmes, *J. Applied Polymer Science*, **2008**, 108, 876-886.
3. S. Kawabata, *J. of the Textile institute* **1990**, 81, 432-447.
4. S. L. Phoenix, J. Skelton, *Textile Research Journal*, **1974**, 44, 934-940.
5. D. W. Hadley, I. M. Ward, J. Ward, *Proceedings of the Royal Society of London*, **1965**, 285, 275-286.
6. J. Singletary, H. Davis, M.K. Ramasubramanian, W. Knoff, M. Toney, *Journal of Materials Science*, **2000**, 35, 573-581.
7. T. Kotani, J. Sweeney, I.M. Ward, *Journal of Materials Science*, **1994**, 29, 5551-5558.
8. S. Abdul Jawad, I. M. Ward, *Journal of Materials Science*, **1978**, 13, 1381-1387.
9. J. Lim, J.Q. Zheng, K. Masters, W. W. Chen, *Journal of Materials Science*, **2010**, 45, 652-661.
10. J. Singletary, H. Davis, M.K. Ramasubramanian, W. Knoff, M. Toney, *Journal of Materials Science*, **2000**, 35, 583-592.
11. M. C. G. Jones, E. LaraCurzio, A. Kopper, D. C. Martin, *Journal of Materials Science*, **1997**, 32, 2855-2871.

[Tapez ici]

12. S. Sockalingam, J.W. Gillespie, M. Keefe, *Int. J. of Solids and Structures*, **2014**, 51, 2504-2517.
13. M. Cheng, W. M. Chen, T. Weerasooriya, *International Journal of Solids and Structures*, **2004**, 41, 6215-6232.
14. M. G. Dobb, R. M. Robson, *Journal of Materials Science*, **1990**, 25, 459-464.
15. R. J. Morgan, C. O. Pruneda, W. J. Steele, *J. Polym. Sci., Part B: Polym. Phys.* **1983**, 21, 1757-1783.
16. M. G. Dobb, C. R. Park, R. M. Robson, *Journal of Materials Science*, **1992**, 27, 3876-3878.
17. C. S. Li, M. S. Zhan, X. C. Huang, H. Zhou, Y. Li, *J. Applied Polymer Science*, **2013**, 128, 1291-1296.
18. M. Grujicic, S. Ramaswami, J. Snipes et al., *Multidiscipline Modeling in Materials and Structures*, **2013**, 9, 462-498.
19. M. Grujicic, S. Ramaswami, J. Snipes et al., *Advances in Materials Science and Engineering*, **2013**, 2013, 1-15.
20. M. Grujicic, S. Ramaswami, J. Snipes et al., *Journal of Materials Engineering and Performance*, **2013**, 22, 3269-3287.
21. J. F. Graham, C. McCague, O. L. Warren, P.R. Norton, *Polymer*, **2000**, 41, 4761-4764.
22. L. Konopasek, J. W. S. Hearle, *J. Applied Polymer Science*, **1977**, 21, 2791-2815.
23. R. J. Young, D. Lu, R. J. Day, W.F. Knoff, H. A. Davis, *Journal of Materials Science*, **1992**, 27, 5431-5440.
24. S. F. Y. Li, A. J. McGhie, S. L. Tang, *Polymer*, **1993**, 34, 4573-4575.
25. M. Panar, P. Avakian, R.C. Blume, K. H. Gardner, T.D. Gierke, H. H. Yang, *J. Polym. Sci., Part B: Polym. Phys.* **1983**, 21, 1955-1969.
26. S. F. Y. Li, A. J. McGhie, S. L. Tang, *Journal of vacuum science and technology*, Part A: Vacuum surfaces and films, **1994**, 12, 1891-1894.
27. Q. P. McAllister, J.W. Gillespie, M.R. VanLandingham, *Journal of Materials Research*, **2012**, 27, 1824-1837
28. T.S. Davison, H.N.G. Wadley, M.J. Pindera, *Composites Engineering*, **1994**, 4, 995-1009.
29. M. Fukuda, H. Kawai, *Textile Research Journal*, **1993**, 63, 185-193.
30. C. Riekel, T. Dieing, P. Engström, L. Vincze, C. Martin, A. Mahen, *Macromolecules*, **1999**, 32, 7852-7865.
31. A. R. Bunsell, J. W. S. Hearle, *Journal of Materials Science*, **1971**, 6, 1303-1311.
32. A. Marcellan, A. R. Bunsell, L. Laiarinandrasana, *Polymer*, **2006**, 47, 367-378.
33. C. LeClerc, A. R. Bunsell, A. Piant, B. Monasse, *Journal of Materials Science*, **2006**, 41, 7509-7523.
34. V. Jauzein, P. Colomban, *Handbook of Tensile Properties of Textile and Technical Fibres*, **2009**, 91, 144-178.
35. C.C. Ma, K.-M. Hung, *International Journal of Mechanical Science*, **2008**, 50, 275-292.
36. P. R. Pinnock, I. M. Ward, J. M. Wolfe, *Proceedings of the Royal Society of London*, **1966**, 291, 267-278.
37. G. Josse, P. Sergot, C. Creton, M. Dorget, *Journal of Adhesion*, **2004**, 80, 87-118.
38. A. Marcellan, A. R. Bunsell, R. Piques, P. Colomban, *Journal of Materials Science*, **2003**, 38, 2117-2123.
39. E. McEwen, *Philosophical Magazine*, **1949**, 40, 454-459.
40. S. Timoshenko, J. Goodier, *Theory of elasticity*, **1951**.
41. E. Pisanova, S. Zhandarov, E. Mäder, I. Ahmad, R. J. Young, *Composites Part A*, **2001**, 32, 435-443.
42. M.G. Northolt, P. DenDecker, S. J. Picken, J. J. M. Baltussen, R. Schlatmann, *Advances in Polymer Science*, **2005**, 178, 100-108.
43. Y. Rao, R. J. Farris, *International Journal of Fatigue*, **2008**, 30, 793-799.
44. S. V. Roth, M. Burghammer, A. Janotta, C. Riekel, *Macromolecules*, **2003**, 36, 1585-1593.
45. S. V. Roth, M. Burghammer, C. Ferrero, A. Diethret, P. Muller-Buschbaum, *Journal of*

[Tapez ici]

- Applied Crystallography*, **2003**, 36, 684-688.
46. G. Mirone, *Engineering Fracture Mechanics*, **2007**, 74, 1203-1221.
47. S. Ran, D. Fang, X. Zang, B.S Hsiao, B. Chu, P. M. Cunniff, *Polymer*, **2001**, 42, 1601-1612.
48. S. Ran, X. Zang, D. Fang, B.S Hsiao, B. Chu, P. M. Cunniff, R. A. Phillips, *Journal of Materials Science*, **2001**, 36, 3071-3077.